Control of supersonic compression corner flow using a plasma actuator ⊘

Zongnan Chen (陳宗南) [iD] ; Jiaao Hao (郝佳傲) [iD] ; Chih-Yung Wen (溫志湧) ✉ [iD]

Check for updates

View Online Export Citation

Articles You May Be Interested In

Thermal effects on the performance of a nanosecond dielectric barrier discharge plasma actuator at low air pressure

Physics of Fluids (January 2023)

Performance and mechanism analysis of nanosecond pulsed surface dielectric barrier discharge based plasma deicer

Physics of Fluids (September 2019)

Characteristics of a nanosecond pulsed dielectric barrier plasma actuator with a surface water film

Phys. Plasmas (January 2022)

Control of supersonic compression corner flow using a plasma actuator

View Online   Export Citation   CrossMark

Zongnan Chen (陳宗南),[1] (iD) Jiaao Hao (郝佳傲),[2] (iD) and Chih-Yung Wen (溫志湧)[2,a] (iD)

AFFILIATIONS

[1]Department of Mechanical Engineering, The Hong Kong Polytechnic University, Hong Kong, China
[2]Department of Aeronautical and Aviation Engineering, The Hong Kong Polytechnic University, Hong Kong, China

[a]Author to whom correspondence should be addressed: cywen@polyu.edu.hk

ABSTRACT

The control performance of a pulsed nanosecond dielectric barrier discharge (NSDBD) plasma actuator with varying pulse voltages and locations on a supersonic compression corner is studied using experiments and numerical simulations. The compression corner with a flat plate length of 60 mm and a ramp angle of $10°$ under laminar flow separation is experimentally investigated in a Ludwieg wind tunnel under a unit Reynolds number of 7.8×10^6 m^{-1} and Mach number of 4. The plasma actuators are placed either upstream or downstream of the separation point, extending in the spanwise direction. The Schlieren technique is used to visualize the shock wave interaction and estimate the propagation speed of the induced shock by the plasma actuator. For the numerical simulations, a one-zone inhomogeneous phenomenological plasma model is adopted to predict key discharge parameters and simulate the fast-heating region. The results show that the reduction of separation bubble length is up to 17% and 45%, respectively, in the cases of upstream and downstream of the separation point under a high applied voltage of 50 kV. The evolution of the flow structures is examined to reveal the underlying control mechanism. The results indicate that the high-speed external fluid is entrained into the original separation region after NSDBD activation upstream of the separation point, resulting in flow reattachment upstream of the corner. The entrained fluid with high momentum compels the main separation to move downstream, accompanied by the fragmentation of the original shear layer. Furthermore, the suppression of the separation region is more effective when the plasma actuator is installed close to the separation region and in the first 200 μs during one pulse, providing a good suggestion for the actuation frequency and installed location.

Published under an exclusive license by AIP Publishing. https://doi.org/10.1063/5.0096511

I. INTRODUCTION

Shock-wave/boundary-layer interaction (SWBLI) is a common phenomenon that occurs in supersonic flow under different conditions. A compression corner, as the basic geometry, has been applied in many supersonic/hypersonic vehicles, including wings, engine inlets, and junctions. The flow physics of SWBLIs over a compression corner depends on whether the state of the incoming boundary layer upstream of the separation is laminar or turbulent. For a laminar interaction, the shock-induced separated flow is highly sensitive to upstream disturbances and can support self-sustained global instabilities.[1,2] Streamwise streaks in heat transfer have been extensively observed, which are essentially the footprints of counterrotating streamwise vortices on the model surface and can cause significantly elevated peak heating with strong spanwise variations and promote boundary-layer transition downstream of the reattachment. Additionally, the laminar separation bubble can oscillate at a low frequency.[3,4] On the other hand, for a turbulent interaction, the separation shock (SS) usually undergoes a back-and-forth motion with

a dominant frequency much lower than that of the energetic eddies in the incoming boundary layer, typically by a factor of 0.1 to 0.01. The low-frequency, large-scale unsteadiness can induce an adverse response of the vehicle structure and a degradation of the aircraft performance. Similar flow phenomena have also been observed in many other canonical configurations. Therefore, it is of interest to reduce the size of the separation region, the strength of the separation shock, and the pressure and heat flux peaks to suppress the generation of counterrotating streamwise vortices and to control the low-frequency unsteady motion of the shock system.

Active flow control via plasma actuators has attracted significant attention because of its flexibility, high efficiency, and fast response.[5] It has been widely used to improve the aerodynamic performance, including the elimination of flow separation on an airfoil, drag reduction, and suppression of the vortex-induced vibration of structures.[6] To effectively control supersonic flow, three types of plasma actuators have been developed in the literature, including plasma synthetic jet

actuators (PSJAs),[7] localized arc filament plasma actuators (LAFPAs),[8] and nanosecond surface dielectric barrier discharge (NSDBD) plasma actuators.[9] Compared with NSDBD plasma actuators, PSJAs have a larger volume occupancy, which increases the actuator mass and limits the spatial arrangement.[10] Furthermore, both PSJAs and LAFPAs[11] can barely maintain uniformity, leading to strong three-dimensional (3D) effects. Therefore, NSDBD plasma actuators have unique superiority and potential in active flow control.

An NSDBD plasma actuator, which is typically composed of four main parts: a high voltage power supply with a nanosecond scale pulse duration, an exposed electrode, an insulated electrode, and a dielectric barrier between these two electrodes, has been applied to a variety of flow control problems. After each discharge pulse, energy deposition occurs quickly in the vicinity of the discharge streamers to form a strong thermalized area. This fast-heating process is essentially a direct excitation of molecules by electron impacts followed by fast quenching or decomposition with "hot" atom formation.[12] Subsequently, an induced shock wave is formed originating at each discharge streamer and propagates to the surrounding air.[13,14] Therefore, the residual heat stemming from the energy deposition and the baroclinic vorticity caused by the interaction between the induced shock wave and the mainstream are the two fundamental characteristics of NSDBD plasma actuators, which have been regarded as the control mechanisms. Notably, NSDBD plasma actuators should be distinguished from alternating current dielectric barrier discharge (AC-DBD) plasma actuators,[15,16] which generate a wall jet-like induced flow and exert a body force on the ambient air (neutrally charged) for flow control.

The application of NSDBD plasma actuators in active flow control has been extensively investigated both experimentally and numerically,[17,18] such as the control of flow separation over an airfoil[19] and a backward-facing step[20] and control of the boundary-layer transition over a flat plate.[21] However, only a few studies have addressed supersonic flow control. An early attempt was made by Nishihara et al.,[22] who used an NSDBD plasma actuator to control a Mach 5 flow over a cylinder. The induced shock wave propagated upstream toward the bow shock and increased the shock stand-off distance by up to 25%. However, the changes in aerodynamic characteristics were not measured. Subsequently, Bisek et al.[23] and Zheng et al.[24] numerically reproduced the flow phenomenon observed by Nishihara et al.[22] using a phenomenological and a self-similar plasma model, respectively. They found that NSDBD plasma actuators were very effective at moving the standing bow shock with a minimal energy budget and that the drag of the cylinder was appreciably reduced. It is indicated that a supersonic maneuver can be achieved by changing the normal force and pitching moment using NSDBD plasma actuators. Kinefuchi et al. experimentally[25] and numerically[26] investigated the control effects of NSDBD on flow separation induced by an impinging oblique shock over a flat plate. Compared with parallel electrodes, the canted electrodes resulting in vorticity production successfully suppressed the boundary-layer separation, which was attributed to momentum transfer from the main flow to the boundary layer.

The aforementioned studies indicate that NSDBD is a novel and potential technology for supersonic flow control. To date, there are only limited studies addressing supersonic SWBLI control using plasma actuators and even fewer using NSDBD plasma actuators. As mentioned before, the flow physics of supersonic SWBLIs depend heavily on the state of the incoming boundary layer. For both laminar and turbulent interactions, the control effects and mechanisms of NSDBD plasma actuators remain unclear. Therefore, as a first step, this paper aims to systematically investigate the understanding of supersonic laminar interaction control. To achieve this objective, experiments are conducted to visualize the shock wave interaction and measure the discharge properties, and numerical analyses are executed to ascertain key information, including the shock systems, skin friction and surface pressure distribution, and temperature evolution of separated flow fields. Moreover, the effect of different locations of plasma actuators is studied to provide an optimized configuration under the given conditions.

II. EXPERIMENTAL AND SIMULATION SETUP
A. Experimental facilities and flow conditions

Experiments were conducted in a supersonic Ludwieg tube at the high-speed thermofluid laboratory of the Hong Kong Polytechnic University with a flow Mach number of 4. The diameter of the nozzle is 300 mm, and the test section has a length of 1000 mm, as shown in Fig. 1(a). The quasi-steady test time is at least 40 ms. Table I lists the
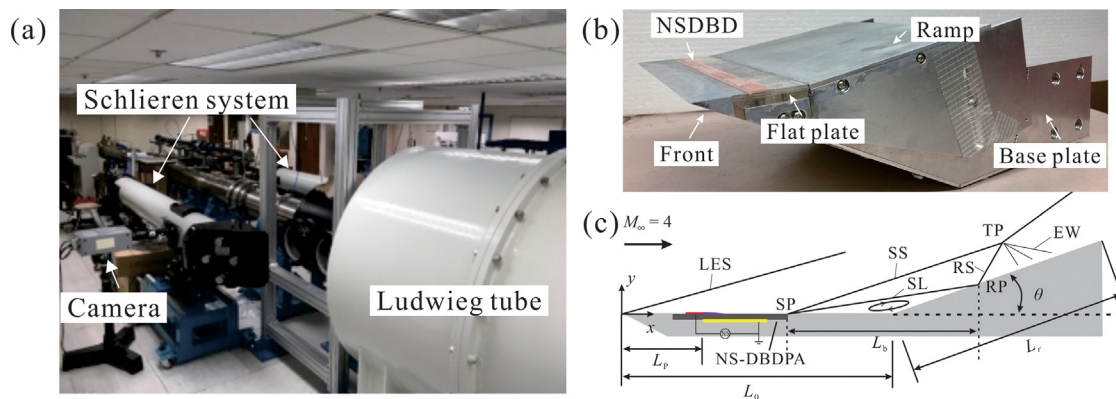
FIG. 1. (a) Ludwieg tube and Schlieren system; (b) schematic of the ramp model with a sharp leading edge and an NSDBD actuator installed; and (c) schematic of the flow structures on the compression corner in a supersonic flow. LES: leading edge shock; SS: separation shock; RS: reattachment shock; EW: expansion wave; SL: separated shear layer; SP: separation point; RP: reattachment point; TP: triple point.

TABLE I. Free stream conditions.

M_∞	Re_∞ (1 m^{-1})	p_∞ (Pa)	U_∞ (ms^{-1})	ρ_∞ (kg m^{-3})	T_∞ (K)
4.0	7.8×10^6	1126	674	0.055	70.7

free stream conditions used in the experimental and numerical studies. The incoming flow has a total pressure of 1710 ± 10 kPa and a total temperature of 297 ± 2 K with a unit Reynolds number of 7.8×10^6.

A Schlieren technique was used to capture the shock structures over the compression corner. This optical diagnostic technique is based on the variation in the refractive medium index due to the difference in the gas density.[27] Our Schlieren system (WCL250G) is composed of the collimation and viewing system [see Fig. 1(a)]. A xenon lamp with an intensity of 80–300 mW/cm^2 was used as a light source. To obtain a high-resolution Schlieren image, a Nikon Nikkor microlens (105 mm f1:2.8D) was used, thereby giving rise to an image spatial resolution of approximately 0.11 mm/pixel. Shock structures were recorded using a high-speed camera (FASTCAM SA-Z type 2100 K-M-32GB) with a resolution of 1024×1024 pixels.

B. Ramp model geometry

The compression corner model comprises a flat plate with a sharp leading edge followed by a ramp. Figures 1(b) and 1(c) depict the main details of the compression corner. The lengths of the flat plate L_0 and the ramp L_r are 60 and 150 mm, respectively. The width of the model is 200 mm. A sharp front with a radius of 0.05 mm is adjoined to the flat plate with an adjustable ramp between 0° and 20° ($\pm$ 0.01°). In the current experimental and numerical studies, a moderate deflection angle of 10° was considered to have a large separation region but without the formation of secondary vortices under the given free-stream conditions. Due to the short running time of the shock tunnel, the surface was assumed to be an isothermal wall with a fixed temperature (T_w) of 297 K.

C. NSDBD plasma actuators

The NSDBD plasma actuator comprises two electrodes (0.01-mm-thick copper) mounted on both sides of a dielectric layer (0.2-mm-thick acrylic). The spanwise length of the actuator is 200 mm, and the widths of the exposed and insulated electrodes are 2 and 10 mm, respectively. There is no gap or overlap between the two electrodes [see Fig. 1(b)]. The actuator was flush placed on an acrylic flat plate to indent the actuator to be as flush as possible with the top surface. The model surface was carefully disposed of to minimize the unevenness due to the exposed electrode and the gaps between different model parts.

A voltage of 25 kV was applied by a nanosecond pulse generator (NPG 18/3500) with a repetition rate of 1000 Hz. The applied voltage and current were measured using a high voltage probe (Tektronix P6015A) and a current shunt probe (Megaimpulse CS-10/500), respectively. In addition, a synchronization system was set up using a synchronizer (BNC Delay Pulse Generator 575–8C). Note that a protective circuit was applied in the trigger system to reduce electromagnetic interference on the data acquisition system.

The NSDBD plasma actuator was placed at different locations above the flat plate. The distance L_P is from the leading edge to the starting location of plasma, which is usually considered the downstream edge of the exposed electrode. The coordinate system is constructed with the origin located at the leading edge of the flat plate, as shown in Fig. 1(c). The x axis is coincident with the flow direction, and the y axis points in the vertical direction. The simulation comprised seven cases that were compared with each other to study the effects of NSDBD at different voltages and streamwise locations. The first case (C0) is the basic state without the actuator. The actuation voltages and actuator locations of other cases are listed in Table II.

III. COMPUTATIONAL DETAILS
A. Plasma model

A one-zone inhomogeneous phenomenological plasma (OZIPP) model[28] of surface NS-DBDPA is adopted in this study to predict the key discharge parameters, such as the plasma length L_D, gas heating energy E_h for a single pulse per unit spanwise width, and its spatial distribution. By integrating the propagation velocity with the pulse rising time τ_r, the plasma length is estimated as a function of the peak voltage V and τ_r. Here, the propagation velocity is acquired by the curve fitting of the data. The energy input per unit spanwise width per pulse E_{in} is assumed to be a function of V and pulse repetition rate f obtained by curve fitting of the experimental data[29] as

$$E_{in}(V,f) = \frac{(0.352\,15 - 0.149\,86 \times 0.998\,11^f)}{(0.352\,15 - 0.149\,86 \times 0.998\,11^{10})} \times (0.185\,17V^0 - 0.0610V^1 + 0.005\,67V^2), \quad (1)$$

where E_{in} is in unit of mJ cm^{-1} and V in kV. Therefore, E_h can be defined as

$$E_h = \eta_h \cdot E_{in}(V, f), \quad (2)$$

where η_h is the efficiency of the energy input converted to gas heating. According to Nudnova's work,[12] η_h can be estimated as 35% during the discharge phase.

The spatial distribution of the gas heating energy density $ED_h(x, y)$, defined as Eq. (3), can be obtained according to the averaged emission intensity [$EI(x/L_D, y/h)$] studied experimentally by Nudnova et al.[12] Note that it is assumed that the energy used to heat the gas is proportional to the intensity of the radiation

$$ED_h(x,y) = E_h(V,f) \cdot \frac{EI(x/L_D, y/h)}{EI_T}. \quad (3)$$

Here, EI_T is the integral value of the distribution function EI, and h is the thickness of plasma according to experiments. The emission intensity distribution EI/EI_T is shown equivalently in Fig. 5(a). Therefore, the power density distribution is defined as

TABLE II. Simulation cases with different parameters.

Case	C0	C1	C2	C3	C4	C5	C6
V (kV)	$\cdots$	25	25	25	50	50	50
L_P/L_0	$\cdots$	0.33	0.50	0.67	0.33	0.50	0.67

$$p_h(x,y) = ED_h(x,y)/\tau_h, \qquad (4)$$

where τ_h is a characteristic heating time. Unfer and Boeuf[30] proposed a two-dimensional (2D) self-consistent numerical model of the discharge and gas dynamics to simulate the fast gas heating process, and a three-species physical model was presented by Wang and Roy[31] to predict the energy and forces. Montello et al.[32] indicated that the fast-heating process in the air occurs on a timescale ($\sim$100 ns) shorter than the characteristic acoustic timescale. Zheng et al.[33] found that a larger τ_h results in a delay of shock initiation and consequently a shock slightly lagging behind that with a smaller τ_h. In this study, τ_h is estimated to be 350 ns, which produces the best quantitative agreement with experiments.[33]

B. Compressible Navier–Stokes equations

The governing equations are the 2D compressible Navier–Stokes equations for a calorically perfect gas written in the following conservation form:

$$\frac{\partial U}{\partial t} + \frac{\partial F}{\partial x} + \frac{\partial G}{\partial y} = \frac{\partial F_v}{\partial x} + \frac{\partial G_v}{\partial y} + S_h, \qquad (5)$$

where

$$U = \begin{pmatrix} \rho \\ \rho u \\ \rho v \\ \rho e \end{pmatrix}, \quad F = \begin{pmatrix} \rho u \\ \rho u^2 + p \\ \rho uv \\ (\rho e + p)u \end{pmatrix},$$

$$F_v = \begin{pmatrix} 0 \\ \tau_{xx} \\ \tau_{xy} \\ u\tau_{xx} + v\tau_{xy} - q_x \end{pmatrix}, \quad G = \begin{pmatrix} \rho v \\ \rho uv \\ \rho v^2 + p \\ (\rho e + p)v \end{pmatrix}, \qquad (6)$$

$$G_v = \begin{pmatrix} 0 \\ \tau_{xy} \\ \tau_{yy} \\ u\tau_{xy} + v\tau_{yy} - q_y \end{pmatrix}, \quad S_h = \begin{pmatrix} 0 \\ 0 \\ 0 \\ p_h \end{pmatrix}.$$

In these expressions, ρ, p, u, and v are the density, pressure, and x and y velocity components, respectively. τ_{ij} is the shear stress tensor modeled under the assumption of a Newtonian fluid and Stokes' hypothesis, and q is the vector of heat conduction modeled according to Fourier's law. Sutherland's law is used to evaluate the dynamic viscosity. The specific heat ratio γ and Prandtl number Pr are set to 1.4 and 0.72, respectively. The effect of the discharge on flow is represented as a heating source in p_h of the energy equation predicted by the OZIPP model. Note that it is set to zero outside the heating time. In the current numerical study, the influence of the interaction of ionic wind is ignored because of the extremely short effective time of body force caused by plasma.

The inviscid fluxes are calculated using the modified Steger–Warming scheme, which can capture strong shocks stably while maintaining sufficient viscous resolution in the boundary layers.[34] The scheme is then extended to a higher order by the monotone upstream-centered schemes for conservation law reconstruction.[35] The viscous fluxes are calculated using a second-order central difference. An implicit line relaxation method[36] is utilized for time integration.

The numerical simulations in this study are performed using a multiblock parallel finite-volume CFD code called PHAROS, which has been successfully applied to supersonic/hypersonic flows over capsule, double-cone, hollow-cylinder/flare,[37] and double-wedge configurations.[38] The flow-field variables are nondimensionalized by L_0, which is considered the characteristic length of the flow. The characteristic time of the flow t_0 is defined as L_0/U_∞, where U_∞ is the velocity of the free stream. Notably, only 2D laminar simulations are considered in the present study.

C. Convergence study

To build confidence of the simulations, the independence of time steps and grid numbers were investigated to maintain convergence and stability. A $M_\infty = 4$ flow over a flat plate with the NSDBD plasma actuator installed at $L_p/L_0 = 0.67$ is simulated (case C6). The boundary conditions are specified as follows: the free-stream conditions are prescribed at the upper and left boundaries. A simple extrapolation outflow condition is used at the exit boundary. For the no-slip wall, isothermal conditions are specified with a wall temperature of 297 K. The distributions of dimensionless temperature T/T_w and overpressure P/P_∞ at $x/L_0 = 0.7$ (where the most gas heating energy is distributed at) and 2 μs after activation are shown in Fig. 2. Four different time steps of 0.1, 0.2, 0.5, and 1 ns under the same grid cells (total of 0.72×10^6) were used to validate the time step independence. It is noted that the maximum temperature along the wall-normal direction is quite susceptible to the time steps, and the temperature distribution shares a similar tendency. Notably, because the heating gas plays a dominant role in flow control, an accurate prediction of the heat input (consequently the temperature distribution) is particularly important. The temperature distribution result of 0.2 ns reaches time step independence. By contrast, the sensitivity of time steps to overpressure is relatively limited. The changes in temperature and pressure with grid refinement are shown in Fig. 2(b). Three grid numbers of 0.18×10^6 (800×225), 0.36×10^6 (800×450), and 0.72×10^6 (1600×450) were used under the same time step (0.2 ns). The meshes are clustered near the leading edge, corner, and wall. Note that the mesh spacing at the wall is 1×10^{-6} m for all three cases, yielding a nondimensional wall distance of $y^+_\text{wall} \approx 0.3$. The present simulations show that the temperature distributions of grid schemes 0.36×10^6 and 0.72×10^6 are almost the same. The two-dimensional flow fields are almost identical for both cases. To ensure the convergence of the simulation, the mesh scheme with a total number of 0.72×10^6 grids and a time step of 0.2 ns are selected for all the simulations presented later in this article.

IV. RESULTS AND DISCUSSION

A. Induced flow in quiescent air by NSDBD

Figure 3(a) shows typical waveforms of the applied voltage and the total current for a positive polarity discharge. The measured peak voltage amplitude is 25 kV, with a duration time of approximately 10 ns. The maximum current is approximately 7.5 A/cm at the first peak during the rise time (within 4 ns) of the voltage. This current peak is caused by charge deposition resulting from discharge near the exposed electrode when the electric field is sufficient to initiate air breakdown. Following the first peak, there is no obvious silent period
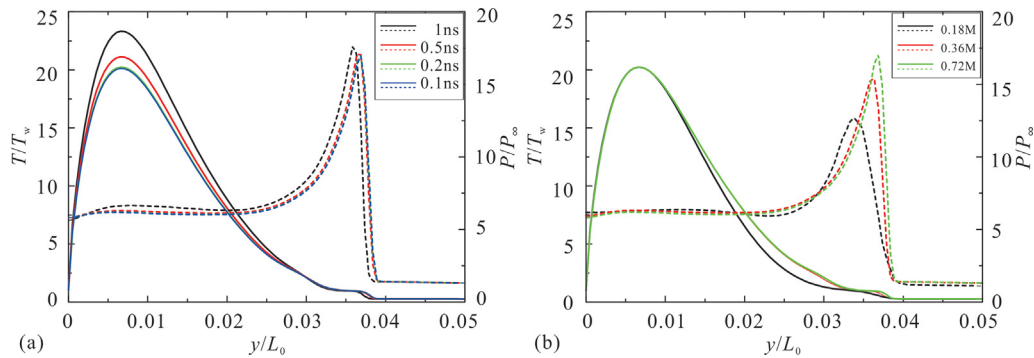
FIG. 2. The distributions of dimensionless temperature (solid lines) and overpressure (dashed lines) for flow over a flat plate at $x/L_0 = 0.7$ and 2 μs after activation, with the change in (a) time steps and (b) grid cells. $L_p/L_0 = 0.67$ (case C6) and $M_\infty = 4$.
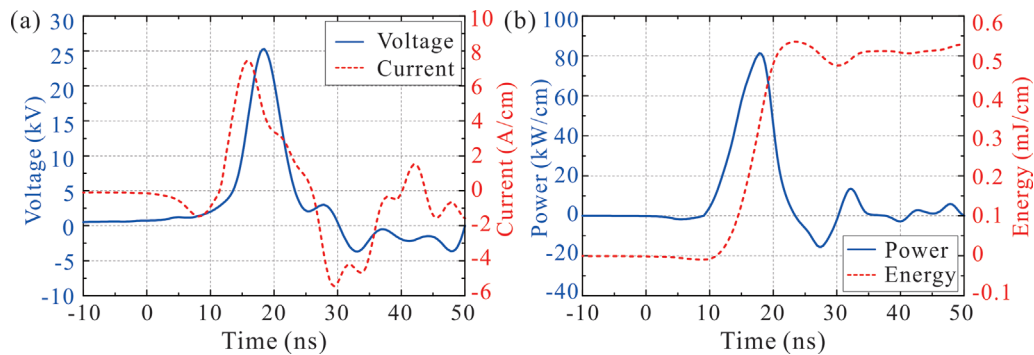

FIG. 3. Electrical aspects of a positive pulse discharge: (a) voltage and current and (b) power and energy.

due to an extremely short duration time. The subsequent negative current peak takes place during the fall time of the voltage where a new discharge occurs with a sufficient potential difference. These two current peaks manifest an asymmetry associated with the completely different discharge regimes.[39] Typical waveforms of the electric power and energy are shown in Fig. 3(b). The power peak results from the power transfer from the supply to the actuator. The energy, integrated by the instantaneous power, reaches an asymptotic quantity of approximately 0.5 mJ/cm at the end of the voltage pulse.

First, the formation of induced flow on a flat plate in quiescent air was studied. To validate the OZIPP model, the conditions based on Zheng's experiment[33] were selected for comparison with numerical simulations. The computational domain is 40 and 20 mm with a grid resolution of 1000×500 in the x and y directions, respectively. The plasma region starts at $x = 0$. The peak voltage, atmospheric pressure, and temperature are set at 40 kV, 101 325 Pa, and 300 K, respectively.

The induced shock wavefront consists of two parts: a semispherical shock and a planar shock, as clearly shown in Fig. 4. The semispherical shock spreads starting from the alignment line of the exposed electrode and insulated electrode, and it is observed to be significantly weaker on the cathode side. The planar shock propagates upward parallel to the discharge streamers, which corresponds to the most gas heating energy. Meanwhile, a rarefaction wave is formed and propagates toward the plate surface. This rarefaction wave is then reflected from the surface and catches up to the induced shock

wavefront. Finally, the induced shock wave is weakened and decelerates to a sonic wave due to the interaction with the rarefaction wave. The good agreement between the experimental and numerical Schlieren images indicates that the OZIPP model can accurately reproduce the propagation of the induced shock and hence the distribution of the gas heating energy implicitly. The simulated distribution of the gas heating energy density is shown in Fig. 5(a). It can be seen clearly
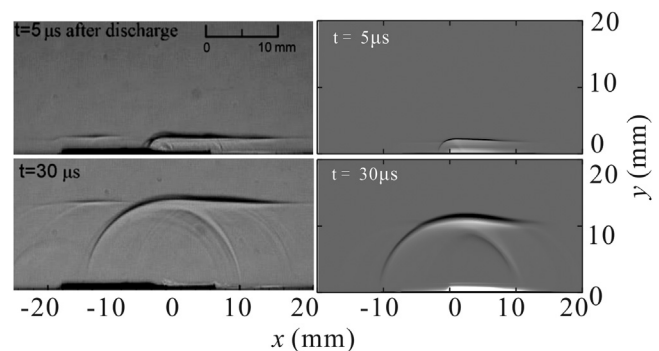
FIG. 4. Comparison of experimental and numerical Schlieren images at different times after actuation under 40 kV (left column shows the experimental Schlieren images by Zheng et al.;[33] right column shows the numerical Schlieren images by the OZIPP model).

(a)

(b)
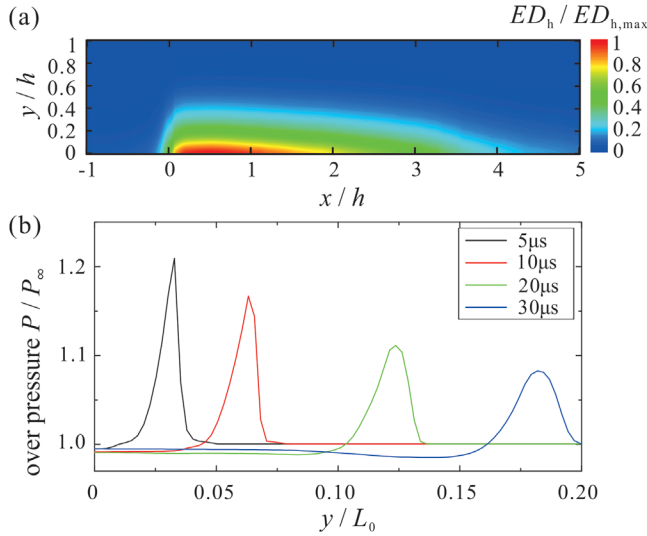
FIG. 5. (a) Nondimensional gas heating energy density distribution and (b) overpressure distributions above the flat plate at $x = 0$ and $t = 5, 10, 20,$ and 30 μs after a pulsed discharge.

that both the longitudinal and vertical energy deposition distributions are nonuniform. The gas heating energy density decreases with the distance from the downstream edge of the exposed electrode in the discharge streamers' direction. Notably, the air density strongly changes in this region due to the fast gas heating, which indicated by the white area near the surface in the numerical Schlieren images (Fig. 4). Figure 5(b) shows the simulated overpressure at the shock wavefront in the cases of 5, 10, 20, and 30 μs after a pulsed nanosecond discharge. It can be used to estimate the shock wave propagation velocity because the peak value indicates the induced shock wavefront location. The perturbation caused by the induced shock is distributed in a thin region and quickly disappears after the induced shock propagates, which exhibits a localized and transient nature.[24]

B. Flow structures over a flat plate

The control effects on a flat plate boundary layer flow at $M_\infty = 4$ are studied first. To compare with cases on the compression corner, the location and applied voltage of NSDBD of case C6 are selected at $L_p/L_0 = 0.67$ and 50 kV. The instantaneous vorticity contours at t^* $= 0.1, 0.15,$ and 0.2 are shown in Figs. 6(a)–6(c), respectively. Here, the dimensional t^* is defined as t/t_0. At the beginning of the activation, the induced vortex can be observed clearly upstream of the heated gas, leading to a separation bubble with an induced separation shock (ISS, marked with a red solid line). The high-momentum fluid is transported into the boundary layer under the entrainment of the induced vortex. Then, the separated flow reattaches to the surface and pushes the heated gas to move downstream. Meanwhile, the induced separation shock interacts with the induced semispherical shock (IS, marked with a blue solid line) by the NSDBD itself, forming a weak reflected expansion wave behind the shock. The streamwise velocity profiles at three different locations (see Fig. 7) become more plentiful in the boundary layer accompanied by a conspicuous decrease above the boundary layer, which indicates momentum exchange between the boundary layer and the upper flow. In the early stage of activation shown by the red dashed line in Fig. 7, the velocity increment in the boundary layer is significant [Fig. 7(b)], but there is a rare difference downstream compared with the baseline [Fig. 7(c)] because the high-speed fluid has not yet propagated there. At the next moment at the same location [blue dashed-dotted line in Fig. 7(c)], the velocity in the boundary layer increases, but this increment decreases at the subsequent moment [green dotted line in Fig. 7(c)]. This indicates that the momentum exchange mainly exhibits a transient timeslot after excitation and a moving region around the heated gas depending on the freestream velocity. Notably, the ISS will decrease the velocity downstream. It can be seen that the velocity defect obtains the least influence of ISS at the location farthest away from it ($x/L_0 = 1.0$) at the same moment, for example, the blue dashed-dotted lines in Figs. 7(a)–7(c). Figures 6(d)–6(f) depict the early stage development of heated gas. The residual heat is impelled downstream and dissipates very quickly. The maximum temperature decreases by approximately half within
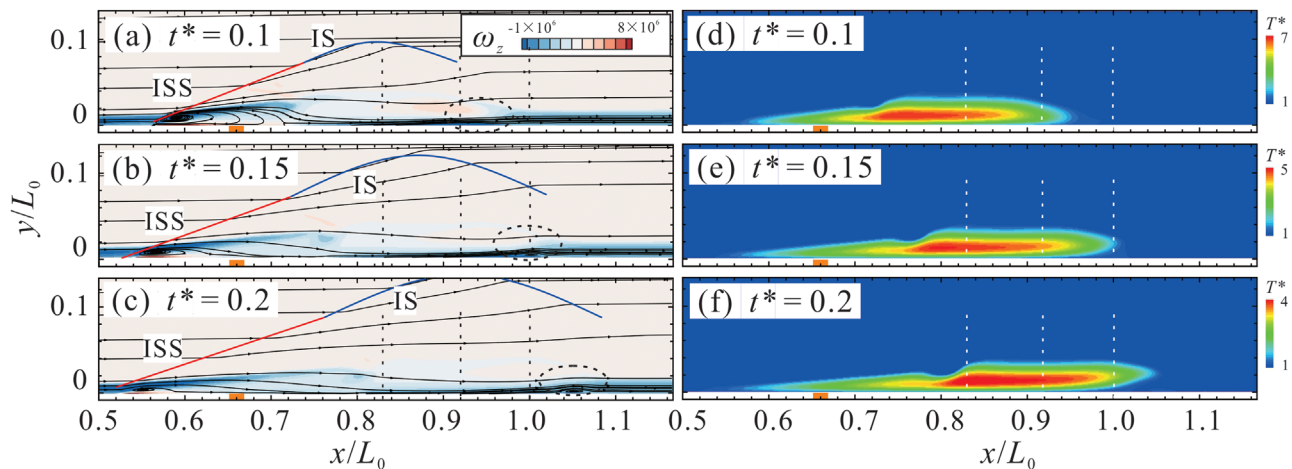
FIG. 6. Contours of instantaneous vorticity ω_z (left column) with superimposed streamlines and nondimensional temperature $T^* = T/T_w$ (right column) at $t^* = $ (a) and (d) 0.1; (b) and (e) 0.15; and (c) and (f) 0.2. The actuator location is at $L_p/L_0 = 0.67$, and it is operated at 50 kV on a flat plate.
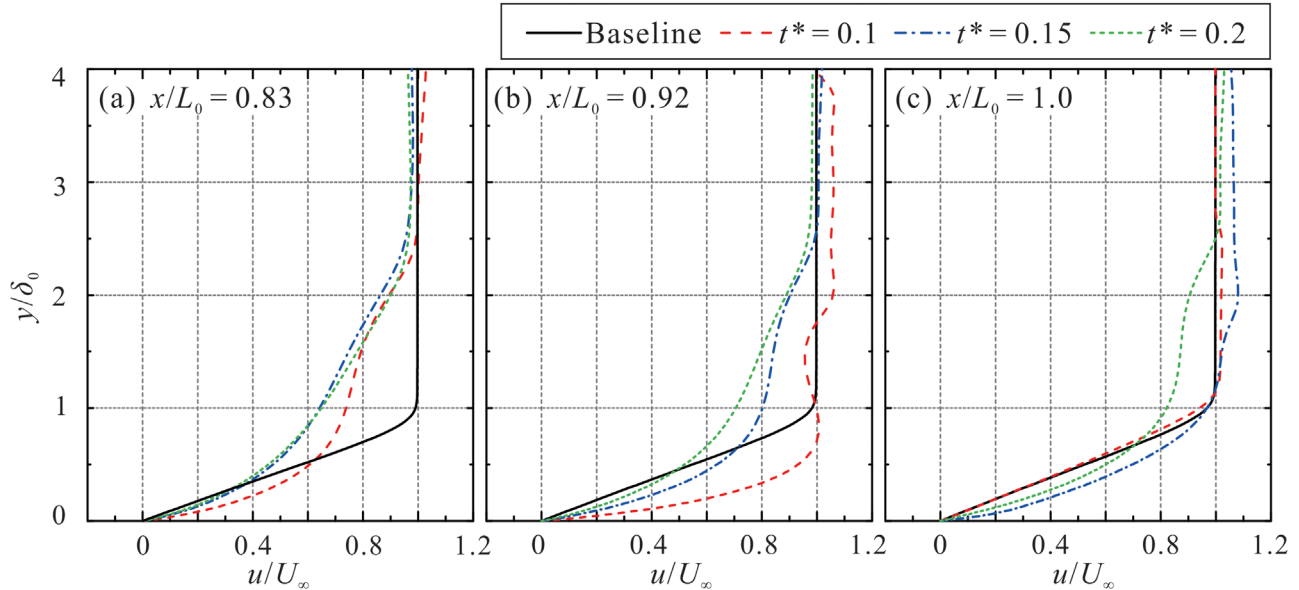
FIG. 7. Streamwise velocity profiles in the vicinity of the boundary layer with and without control at (a) $x/L_0 = 0.83$, (b) $x/L_0 = 0.92$, and (c) $x/L_0 = 1.0$.

$10\,\mu s$. Notably, a perturbation occurs at the front edge of the residual heat, which is marked with an open circle in the left column of Fig. 6. It seems to be generated by a pure thermal perturbation other than the propagation of the induced shock (IS). As shown in Fig. 6(a), the shock-induced perturbation moves a distance away from the discharge region and is presented as a distortion of streamlines behind the shock front. This implies that the flow field can be disturbed by the propagation of IS, but the perturbance is transient and localized in the vicinity of the IS front. It has little contribution to the changes in the flow field when the IS has moved outside the plasma region.

C. SWBLIs on the compression corner

The compression corner comprises a flat plate with a sharp leading edge followed by a ramp. Figure 1(c) schematically depicts the main details of a separated supersonic flow over the compression corner. As shown in Figs. 8(a) and 8(b), the light curves near the surface, which begin at the leading edge and extend downstream, indicate the development of the boundary layer. The numerical and experimental results agree well with each other. The flat plate boundary layer separates from the surface, caused by the sufficiently large pressure increase due to the ramp. Then, it reattaches at the downstream ramp, causing
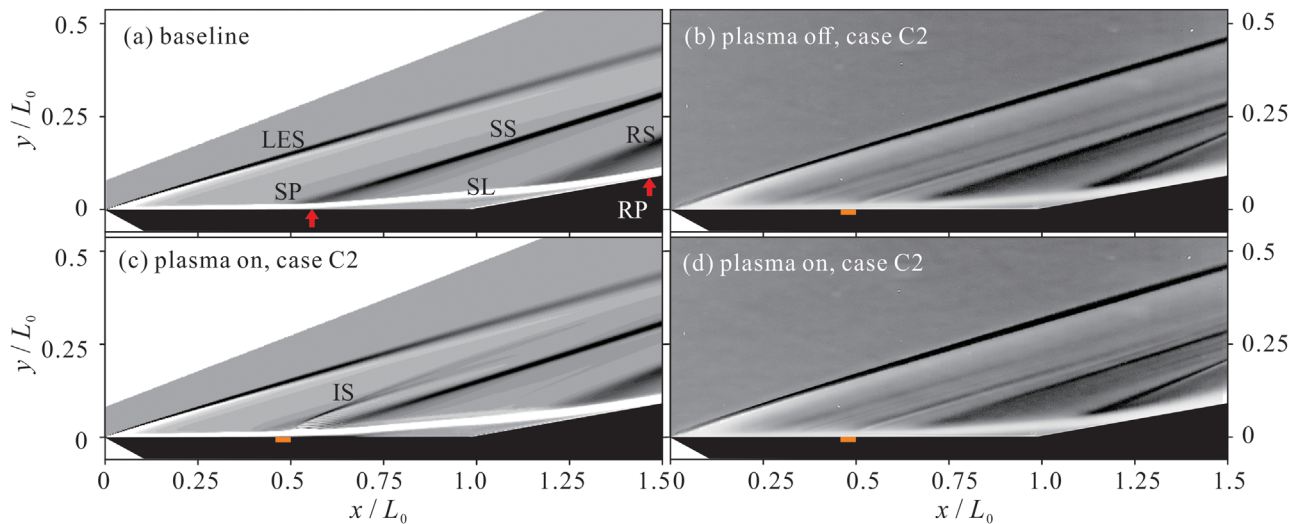

FIG. 8. (a) Numerical Schlieren image of the baseline case (steady); (b) time-averaged experimental Schlieren image of the plasma-off case within one period of case C2; (c) time-averaged numerical Schlieren image of the plasma-on case within the first 0.2 period ($t^* = 2.25$) of case C2; and (d) time-averaged experimental Schlieren image of the plasma-on case within the first 0.2 period ($t^* = 2.25$) of case C2.
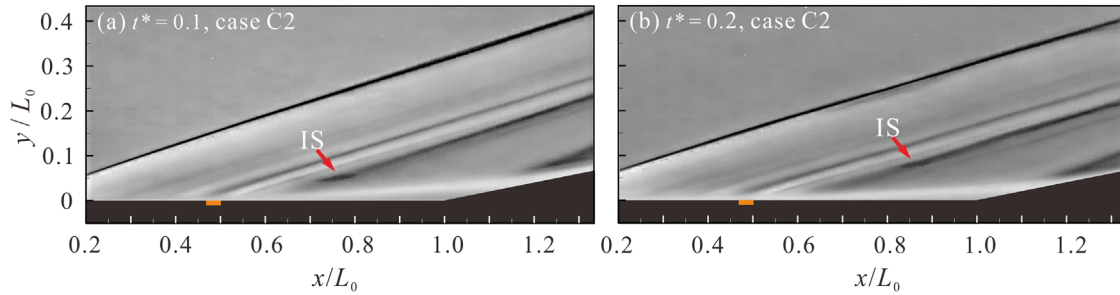
FIG. 9. Shock propagation from NSDBD in the case of C2 at $t^* =$ (a) 0.1 and (b) 0.2.

a reattachment shock (RS). An expansion wave (EW) emanates from the triple point (TP) where the separation shock (SS) caused by the separated boundary layer and reattachment shocks intersect. Below the separated shear layer, between the separation point (SP) and reattachment point (RP), a recirculation bubble forms. The size of the recirculation bubble is strongly affected by the deflection angle, Mach number, and Reynolds number of the incoming flow.[40] In this study, the separation bubble is narrow with a small separation shock angle, which represents a stable laminar separated flow. Note that a secondary eddy will appear in the recirculation region under a large deflection angle, and multiple eddies will form as the deflection angle further increases. According to the global instability analysis of Hao *et al.*,[41] the prediction of the stability boundary in terms of a scaled ramp angle is $\alpha^* = 4.59$ for the current flow conditions, under which the secondary eddy begins to emerge. In this study, the scaled ramp angle α^* is 4.2, which is less than the above critical value of 4.59.

The time-averaged Schlieren images are shown in Figs. 8(c) and 8(d) to investigate the shock system after control, taking case C2 as an example. Note that the field of view of Schlieren did not include the expansion wave and the triple point. It should be pointed out that although the height of the exposed electrode is only 0.02 mm, this small embossment also generates a weak shock wave in the experiment [see Fig. 8(b)]. Chuvakhov and Radchenko[42] indicated that the small height of roughness elements (in their case, less than 0.6 mm) does not affect the separated flow much and only results in a shock wave. This is further proven by the fact that the separated shock angle does not have an obvious change in both the simulation and experiment, calculated by the linear regression of the sampling points in the Schlieren images. In addition, the accumulation of residual heat cannot be observed in experimental Schlieren images because the activated frequency of the plasma actuator is too low compared with the characteristic frequency (L_0/U_∞). The residual heat has been totally convected downstream of the separation region, and the separated flow has restored to the uncontrolled state before the next pulse. The repetition frequency of plasma actuator, which may play a significant role in the control, will be studied in the future.

Figure 9 shows the Schlieren images at $t^* = 0.1$ and 0.2 when the NSDBD plasma actuator is installed at $L_p/L_0 = 0.5$ (case C2). The induced shock (IS) moves downstream and interacts with the separated shock wave. Sweeping by the induced shock wave, the strength of the separated shock seems to be locally perturbed and decreased. Because the experiments were conducted at a low applied voltage, the separation bubble showed little change, which can also be observed in

the simulation results. The simulated and experimental Schlieren images rarely show obvious changes for other actuation position cases, which are not shown here to save space. To determine the control mechanism, more details are analyzed in the simulation study.

D. Control effects on the separation region

To compare the control effects on the size of the separation region, the time-averaged flow field was studied. Regarding the underlying control mechanism, the evolution of flow after one discharge pulse is investigated in Sec. IV E. The averaged time slot was set within $t^* = 2.25$ when the flow has recovered to be steady. A typical separation flow field over a supersonic compression corner is presented by the streamlines in Fig. 10. The separation points (SP), reattachment points (RP), and locations of plasma actuators are marked by closed circles and squares, respectively. The contours of the dimensional streamwise velocity $\overline{u}/U_\infty$ are plotted in Fig. 10(a), where $\overline{u}$ is the local streamwise velocity of steady flow. The separation bubble region is relatively large when the flow is not controlled [see Fig. 10(a)]. The shear flow separates at $x/L_0 = 0.58$ and reattaches at $x/L_0 = 1.42$ with a separation bubble length of $L_b/L_0 = 0.84$. When the actuator is activated at $L_p/L_0 = 0.33$ in the case of C4 [see Fig. 10(b)], the bubble size slightly shrinks, and the SP moves downstream to $x/L_0 = 0.62$. In the
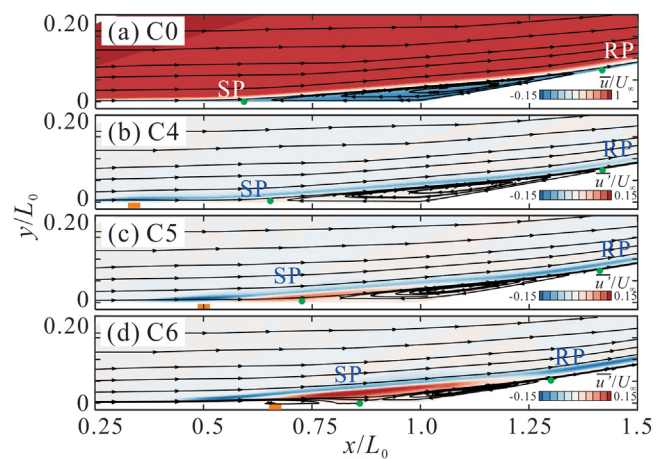

FIG. 10. Time-averaged contours of (a) normalized streamwise velocity ($\overline{u}/U_\infty$) for case C0 and normalized streamwise velocity fluctuation ($\overline{u'}/U_\infty$) for cases (b) C4; (c) C5; and (d) C6 with streamlines superimposed.
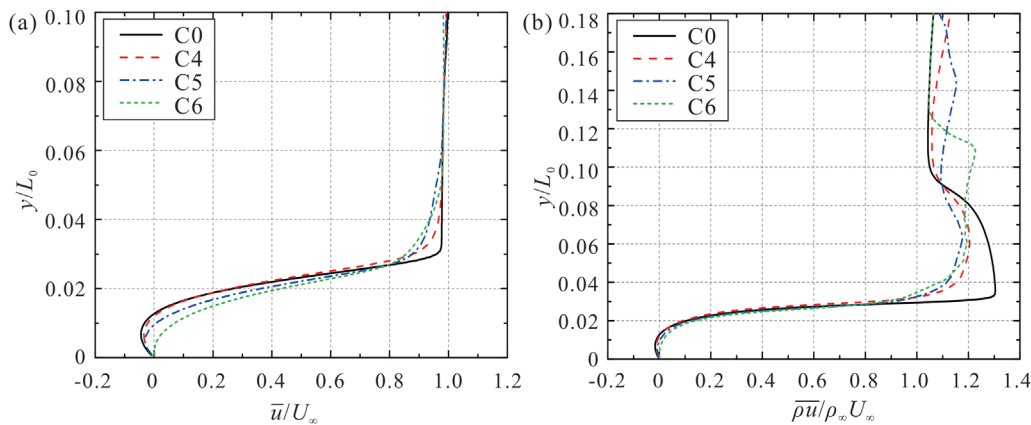
FIG. 11. Profiles of (a) normalized time-averaged velocity $\overline{u}/U_\infty$ and (b) normalized time-averaged mass flux $\overline{\rho u}/\rho_\infty U_\infty$ streamwise at $x/L_0 = 0.8$.

case of C5, where the location of plasma is close and upstream of the initial SP, reductions in the main separation bubble region are also observed [see Fig. 10(c)], and the corresponding SP retards to $x/L_0 = 0.72$. Similar to case C5, when the actuator is arranged close to but downstream of the initial SP at $L_p/L_0 = 0.67$, the SP moves downstream to $x/L_0 = 0.89$, but the RP advances to $x/L_0 = 1.35$, resulting in significant suppression of L_b/L_0 to 0.46. In general, the reduction of separation bubble length is obvious in the cases of C5 and C6 (up to 17% and 45%, respectively). Actually, an initial induced separation exists upstream of the excitation position, which will be discussed in Sec. IV E.

The contours of the time-averaged dimensionless streamwise velocity fluctuation $\overline{u'}/u_\infty$ are plotted in Figs. 10(b)–10(d), where $\overline{u'}$ is defined as $\overline{u-u_0}$. After control, the streamwise velocity component decreases upstream of the initial shear layer and then obviously increases downstream, especially in the case of C6. This result implies momentum exchange upstream and downstream of the initial shear layer. The high-speed fluid with more momentum is transferred to the separation region. This enhances the flow capability to withstand an adverse pressure gradient, resulting in the shrinkage of the separation bubble. To further demonstrate this, profiles of streamwise velocity at $x/L_0 = 0.8$ are plotted in Fig. 11(a). A prominent velocity defect with a

negative value is observed in the baseline case, which represents a typical separation flow. After control, the velocity increases near the wall, which benefits from the momentum supplement by the upper high-speed fluid. It can be seen in Fig. 11(b) that the most momentum supplement from the upper flow at the selected position is observed in the C6 case. However, the time-averaged momentum increase is not obvious in the boundary layer because of the low-density region caused by the gas heating process and the short period when the separation is totally suppressed. Therefore, the prediction of the potential control authority of the NSDBD here should be made with caution. The control mechanism may be linked to the actuation position and its local specific fluid characteristics. A more appropriate excitation position may lead to a better control effect under the same energy input. Analyses of surface pressure and skin friction are helpful to understand the local fluid status after control and elucidate the control mechanism.

Figure 12 shows the distributions of the skin friction coefficient for different actuator locations and applied voltages. The SP and RP of the main separation bubble are indicated by solid open circles. Inside the separation region, there are two local minima of C_f and a local skin friction peak between these two minima near the corner. Downstream of the reattachment point, the skin friction rises to another peak value
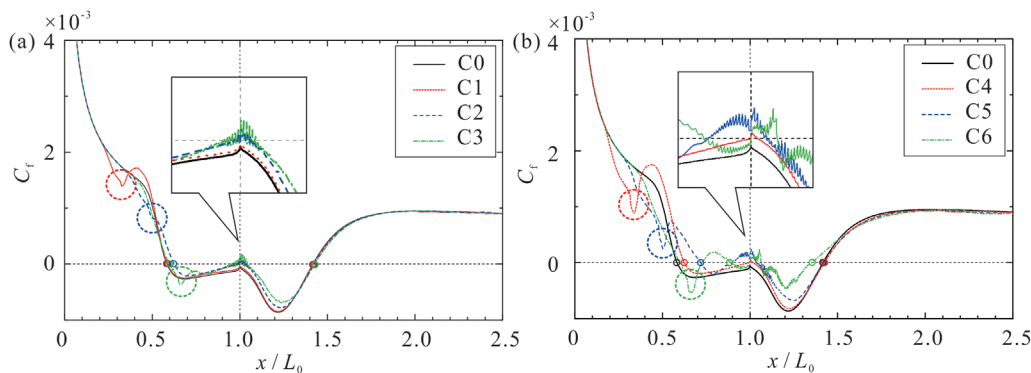

FIG. 12. Distributions of the time-averaged skin friction coefficient for different actuator locations at (a) 25 and (b) 50 kV.
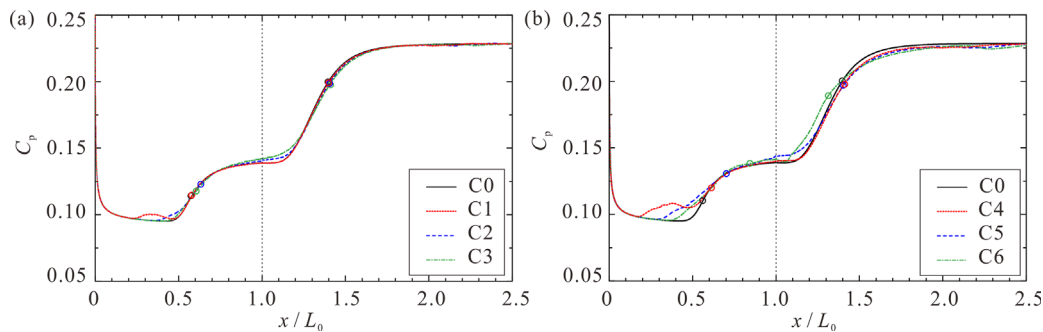
FIG. 13. Distributions of the time-averaged surface pressure coefficient for different actuator locations at (a) 25 and (b) 50 kV.

and then decreases gradually. A sharp valley, marked in a dotted circle, can be seen clearly in all controlled cases. This is caused by the heat impulse originating from the fast heating of pulsed discharge. The actuation drops the surface friction upstream of the heating region and subsequently results in a rebound downstream of it, which is consistent with the process of initial separation and reattachment due to the induced vortex. For the cases of applied voltage at 25 kV [see Fig. 12(a)], the separation bubble sizes show limited changes. However, with the higher applied voltage at 50 kV, the separation bubble strongly shrinks. As the excitation position moves close to the corner, the process becomes more complicated. Inside the separation bubble, the downstream local minimum increases after control. It is indicated that the effects of the NSDBD diminish the accelerated process caused by the favorable pressure in the recirculation boundary layer. After control, the local peak near the corner (see the enlarged region in Fig. 12) becomes positive except in case C1, indicating the emergence of vortices in the separation region. The fluctuating positive peaks illustrate the vortices' time evolution.

The distributions of the surface pressure coefficient for different actuator locations and voltages are shown in Fig. 13. The surface pressure begins to increase upstream of the SP controlled by the free-interaction process.[41] The flow expansion caused by the fast-heating

process increases the local C_p, resulting in the SP moving downstream. Notably, when the upstream actuation is far from the SP, C_p will drop slightly before it rises again. The rise is followed by a plateau region, the value of which increases slightly after control. The pressure rises again near the reattachment point and reaches its peak value mainly determined by the oblique shock theory.

E. Discussion of the control mechanism

To gain the underlying control mechanism, the instantaneous flow field after the first pulse discharge is investigated in all cases. Taking the example of case C5 first, the normalized streamwise velocity contours overlaid with the streamlines are visualized in Fig. 14. At $t^* = 0.1$, 9 μs after the beginning of the discharge, the induced vortices form the initial separation bubble near the original separation point of the boundary layer, which is observed clearly in Fig. 14(a). Its formation is attributed to the interaction between the freestream and the local flow expansion caused by the fast-heating process. Downstream of the bubble, the external high-speed fluid is entrained into the original separation region, resulting in flow reattachment upstream of the corner. The entrained fluid with high momentum compels the main separation to move downstream, accompanied by the fragmentation
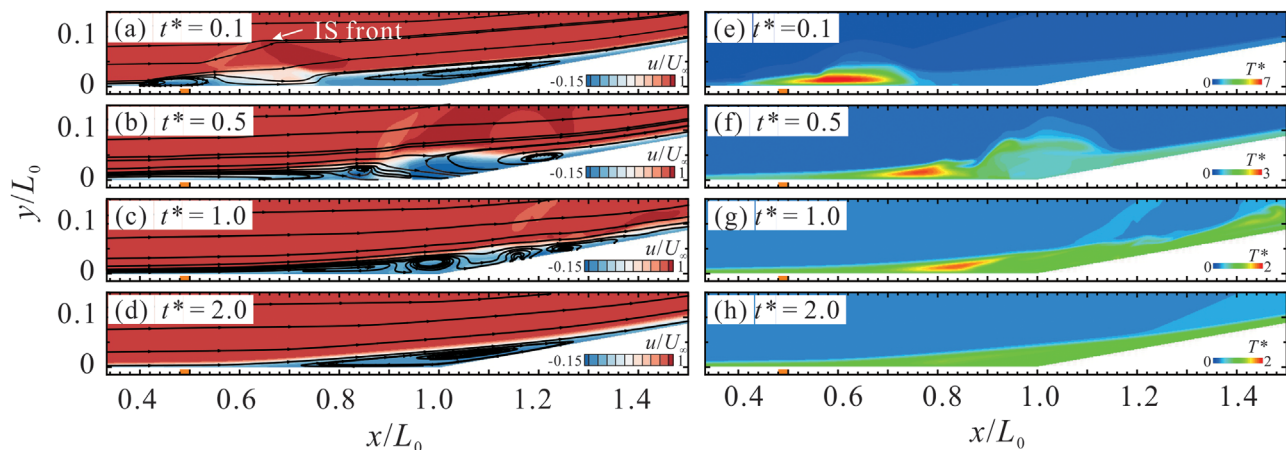

FIG. 14. Contours of instantaneous normalized streamwise velocity u/U_∞ (left column) with streamlines superimposed and nondimensional temperature T^* (right column) at $t^* =$ (a) and (e) 0.1; (b) and (f) 0.5; (c) and (g) 1.0; and (d) and (h) 2.0. The actuator location is at $L_p/L_0 = 0.5$ and $V = 50$ kV (case C5).

of the original shear layer. Note that, at this time, the flow field on the ramp, for example, the RP, is not affected because the perturbed fluid has not propagated downstream to the corner. Subsequently, at $t^* = 0.5$ [see Fig. 14(b)] when the entrained fluid passes through the corner, the original shear layer is destroyed, and multiple vortices emanate in the original separation region caused by the impact between the entrained high-speed fluid and the reverse flow coming from the reattachment point. The reattachment point is pushed downstream transitorily and then fluctuates on the ramp surface near the original reattachment point in the form of small vortices fragmented in the separation region [see Fig. 14(c)]. At the same time, the original induced separation bubble is elongated, flattened, and moves downstream to coalesce with fragmented vortices. At $t^* = 2$ [see Fig. 14(d)], the main separation bubble forms again. At this time, the bubble length is still shorter than that in the steady case and recovers to its original size gradually. Case C2, which has a lower energy input but the same excitation position, shares similar control authority with weaker effects.

Correspondingly, Figs. 14(e)–14(h) show the "moving heat" evolution at different t^*. Here, the dimensionless temperature T^* is defined as T/T_w. It can be seen in Figs. 14(a) and 14(e) that the high-momentum fluid is brought into the separation region with the heated fluid traveling downstream of the separation point. Under a sufficient mixture with the downstream fluid, the heat dissipates in the shear flow very quickly. The process of destruction and reattachment of the shear layer seems to be in accordance with the evolution of the heated fluid transmitted downstream. These results indicate that thermal perturbation may have the greatest contribution. The energy deposition during the discharge poses a significant change in temperature, which also changes the local density and viscosity. This drastic thermal perturbation, such as the temperature gradient, may excite inherent flow instability, such as Kelvin–Helmholtz instability of the shear layer, and eventually induce the generation of vortices.[43] Meanwhile, the induced shock during the fast-heating process may make little contribution to the induced vortices in the initial separation bubble. First, the perturbation to flow properties caused by the induced shock is limited in a narrow region behind the shock front. Second, the induced shock will decay very quickly. It can be seen in Fig. 14(a) that at $t^* = 0.1$, the induced shock wave front has moved to $y/L_0 = 0.1$ and is outside the

separation region. The streamlines are deformed across the induced shock. At $t^* = 0.5$, after the induced shock decays rapidly, the flow field swept by the induced shock wave has returned almost to its steady state. The heated fluid propagates into the shear layer, while the induced wavefront has traveled far away from the separation region. This is due to the appreciable velocity difference between the external and separated regions. Apparently, the perturbated flow field highly depends on both the freestream velocity and induced shock intensity. These results imply that the influence on the separation region by the induced shock is transient and limited. The lasting effects may be caused by momentum entrainment into the separation region due to residual heat-induced vortices.

For cases C1 and C4, in which the excitation position is far upstream of the main separation region, the control effects are limited. In the beginning, the entrained high-momentum fluid is brought into the boundary layer before the main separation bubble. Then, it has a weak impact on the separation region and finally dissipates in the shear layer. Although the main separation bubble is broken, the crushed structures are recombined quickly with little effect on the separation point [see Fig. 15(b)]. In this case, the heat dissipates in the boundary layer, and high-momentum fluid is hardly transferred into the separated region, which only leads to a weak impact on the main separation bubble.

Compared with these four cases hereinbefore, the actuators in cases C3 and C6, which are installed downstream of the original separation point, may function in a different way. When the energy input is low in the case of C3, only a small amount of upper high-speed fluid is brought into the separation region, and the attached flow cannot be sustained for a long time. Moreover, the shear layer cannot be totally destroyed. The separation bubble grows due to the heating effects in the separation region for a short time at the beginning of activation [see Fig. 16(b)]. That is why there is a larger time-averaged L_b in the case of C3 compared with C2 [see Fig. 13(a)]. However, in the case of C6, the drastic discharge at a higher voltage than C3 causes a more lasting and stronger momentum input in the separation region [see the contours in Fig. 10(d)], resulting in a more complicated perturbation in the shear layer. In Fig. 16(e), the high-momentum fluid impacts the reversed flow and totally breaks the original separated shear layer.
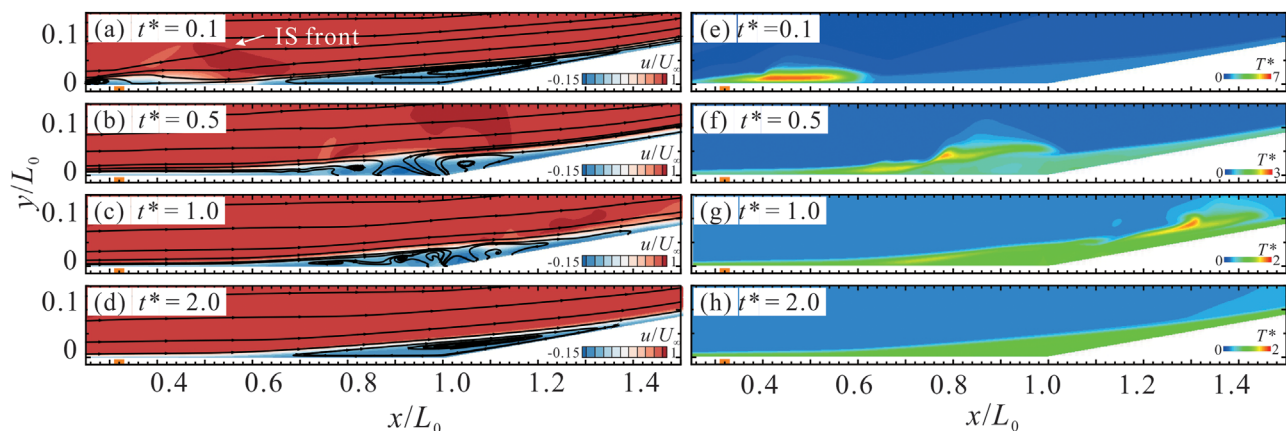
FIG. 15. Contours of instantaneous normalized streamwise velocity u/U_∞ (left column) with streamlines superimposed and nondimensional temperature T^* (right column) at $t^* =$ (a) and (e) 0.1; (b) and (f) 0.5; (c) and (g) 1.0; and (d) and (h) 2.0. The actuator location is at $L_p/L_0 = 0.33$ and $V = 50$ kV (case C4).
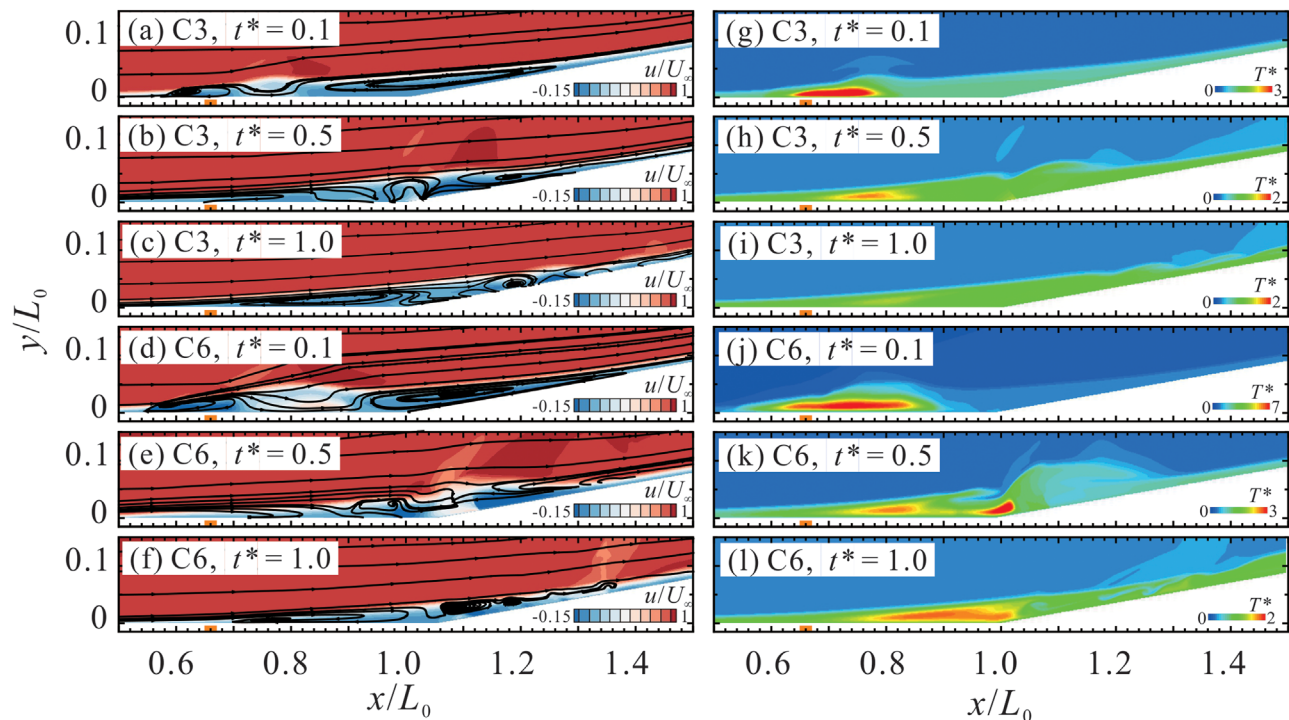
FIG. 16. Contours of instantaneous normalized streamwise velocity u/U_∞ (left column) with streamlines superimposed and nondimensional temperature T^* (right column), at t^* = (a) and (g) 0.1; (b) and (h) 0.5; (c) and (i) 1.0 of case C3 and (d) and (j) 0.1; (e) and (k) 0.5; and (f) and (l) 1.0 of case C6. The actuator location is at $L_p/L_0 = 0.67$ (cases C3 and C6).

More high-momentum fluid is brought into the separation region to withstand the adverse pressure gradient. Note that, caused by the coaction of both the adverse pressure gradient and heating effects, the induced separation bubble is larger than in other cases. In a time-averaged result, the original separation region seems to be divided into two parts, an induced separation bubble and the main separation, which is significantly shrunken.

It is concluded that sufficient momentum exchange in the separation region caused by the induced vortex is the control mechanism. The excitation location is a dominant parameter depending on the specific flow system and its local fluid characteristics. In addition, Zheng et al.[43] proposed that the residual heat can be considered a remarkable "moving perturbation source" whose influence region can be extended with advection. A new perturbation in the boundary layer is generated downstream of the initially induced vortices with the advection of residual heat. In this study, a similar perturbation is also observed in the simulation on a flat plate under supersonic flow conditions. The results indicate that the residual heat triggers the initial vortices and plays a dominant role in the control of a separated flow. Moreover, the supersonic flow manifests a more resilient characteristic to the thermal impact, and the shear layer breakup procedure is more complex. A more appropriate excitation position strongly increases the control efficiency.

V. CONCLUSION

In this paper, the flow control of an NSDBD on a laminar supersonic compression corner is investigated in detail to explore the probable control mechanism. First, conventional high-speed Schlieren imaging was used to visualize the shock wave systems. A one-zone inhomogeneous phenomenological plasma model was adopted to simulate the fast-heating process of discharge. The flat plate simulation demonstrated that there exists a momentum exchange between the upper external flow and the boundary layer. The high-momentum fluid is entrained through the induced vortex caused by the discharge. A similar acceleration was observed in the ramp cases, which can increase the ability to resist the adverse pressure gradient in the separation region. Moreover, the separated shear layer is broken under the collision of high-speed fluid upstream, which can bring more kinetic energy into the separation region. Hence, choosing the most appropriate position based on its local fluid characteristics will strongly increase the control efficiency. For a supersonic compression corner, excitation near the separation point achieves a higher efficiency in suppressing the separation bubble. This study suggests that the NSDBD plasma actuator is a feasible and promising method for separation control in a laminar supersonic flow. It is expected that this study can provide some guidance for further investigation on the control efficiency and inspire more ideas on the application of this control technology.

AUTHOR DECLARATIONS

Conflict of Interest

The authors have no conflicts to disclose.

Author Contributions

Zongnan Chen: Conceptualization (lead); Data curation (lead); Formal analysis (lead); Investigation (equal); Methodology (equal); Writing—original draft (lead); Writing—review and editing (equal). **Jiaao Hao:** Conceptualization (equal); Funding acquisition (equal); Investigation (equal); Methodology (lead); Resources (equal); Supervision (equal); Writing—original draft (supporting); Writing—review and editing (supporting). **Chih-Yung Wen:** Conceptualization (equal); Funding acquisition (lead); Investigation (equal); Project administration (lead); Resources (lead); Supervision (lead); Writing—original draft (supporting); Writing—review and editing (equal).

DATA AVAILABILITY

The data that support the findings of this study are available from the corresponding author upon reasonable request.

REFERENCES

[1]V. Theofilis, "On the origins of unsteadiness and three-dimensionality in a laminar separation bubble," Philos. Trans. R. Soc. London, Ser. A **358**, 3229–3246 (2000).

[2]V. Theofilis, "Global linear instability," Annu. Rev. Fluid Mech. **43**(1), 319–352 (2011).

[3]J. C. Robinet, "Bifurcations in shock-wave/laminar-boundary-layer interaction: Global instability approach," J. Fluid Mech. **579**, 85–112 (2007).

[4]S. Cao, J. Hao, I. Klioutchnikov, H. Olivier, and C.-Y. Wen, "Unsteady effects in a hypersonic compression ramp flow with laminar separation," J. Fluid Mech. **912**, A3 (2021).

[5]Z. Chen, L. Shen, and C.-Y. Wen, "Flow control on a bluff body using dielectric barrier discharge plasma actuators," AIAA J. **57**(7), 2670–2674 (2019).

[6]Z. Chen and C.-Y. Wen, "Flow control of a D-shaped bluff body using different DBD plasma actuators," J. Fluids Struct. **103**, 103292 (2021).

[7]M. Tang, Y. Wu, H. Wang, S. Guo, Z. Sun, and J. Sheng, "Characterization of transverse plasma jet and its effects on ramp induced separation," Exp. Therm. Fluid Sci. **99**, 584–594 (2018).

[8]F. Liu, H. Yan, W. Zhan, and Y. Xue, "Effects of steady and pulsed discharge arcs on shock wave control in Mach 2.5 flow," Aerosp. Sci. Technol. **93**, 105330 (2019).

[9]Y. Wang, H. Zhang, Y. Wu, Y. Li, and Y. Zhu, "Supersonic compressor cascade flow control using plasma actuation at low Reynolds number," Phys. Fluids **34**(2), 027105 (2022).

[10]A. Belinger, N. Naudé, J. P. Cambronne, and D. Caruana, "Plasma synthetic jet actuator: Electrical and optical analysis of the discharge," J. Phys. D **47**(34), 345202 (2014).

[11]C. A. Brown, "Scalability of the localized arc filament plasma actuators," paper presented at the 29th AIAA Aeroacoustics Conference, Vancouver, BC, Canada, 5–7 May 2008.

[12]M. Nudnova, S. Kindusheva, and N. Aleksahdrov, "Rate of plasma thermalization of pulsed nanosecond surface dielectric barrier discharge," paper presented at the 8th AIAA Aerospace Sciences Meeting Including the New Horizons Forum and Aerospace Exposition, Orlando, FL, 2010.

[13]G. Correale, R. Winkel, and M. Kotsonis, "Energy deposition characteristics of nanosecond dielectric barrier discharge plasma actuators: Influence of dielectric material," J. Appl. Phys. **118**(8), 083301 (2015).

[14]C. Zhang, B. Huang, Z. Luo, X. Che, P. Yan, and T. Shao, "Atmospheric-pressure pulsed plasma actuators for flow control: Shock wave and vortex characteristics," Plasma Sources Sci. Technol. **28**(6), 064001 (2019).

[15]L. Shen, Z. N. Chen, and C.-Y. Wen, "Thermal effect on the performance of an alternating-current dielectric-barrier-discharge plasma actuator," AIAA J. **58**(8), 3368–3377 (2020).

[16]W. Hui, H. Zhang, J. Wang, X. Meng, and H. Li, "Heat transfer characteristics of plasma actuation in different boundary-layer flows," Phys. Fluids **34**(3), 034110 (2022).

[17]B. Wei, Y. Wu, H. Liang, J. Chen, G. Zhao, M. Tian, and H. Xu, "Performance and mechanism analysis of nanosecond pulsed surface dielectric barrier discharge based plasma deicer," Phys. Fluids **31**(9), 091701 (2019).

[18]Y. Liu, C. Kolbakir, A. Y. Starikovskiy, R. Miles, and H. Hu, "An experimental study on the thermal characteristics of NS-DBD plasma actuation and application for aircraft icing mitigation," Plasma Sources Sci. Technol. **28**(1), 014001 (2019).

[19]D. V. Roupassov, A. A. Nikipelov, M. M. Nudnova, and A. Y. Starikovskii, "Flow separation control by plasma actuator with nanosecond pulsed-periodic discharge," AIAA J. **47**(1), 168–185 (2009).

[20]Y. D. Cui, Z. J. Zhao, J. Li, J. G. Zheng, and B. C. Khoo, "Flow separation control over a ramp with nanosecond-pulsed plasma actuators," paper presented at the Proceedings of 30th International Symposium on Shock Waves, 2017.

[21]Z.-J. Zhao, Y. D. Cui, J.-M. Li, J.-G. Zheng, and B. C. Khoo, "On the boundary flow using pulsed nanosecond DBD plasma actuators," Mod. Phys. Lett. B **32**(12n13), 1840035 (2018).

[22]M. Nishihara, K. Takashima, J. W. Rich, and I. V. Adamovich, "Mach 5 bow shock control by a nanosecond pulse surface dielectric barrier discharge," Phys. Fluids **23**(6), 066101 (2011).

[23]N. J. Bisek, J. Poggie, M. Nishihara, and I. Adamovich, "Hypersonic flow over a cylinder with a nanosecond pulse electrical discharge," J. Thermophys. Heat Transfer **28**(1), 18–26 (2014).

[24]J. G. Zheng, Y. D. Cui, J. Li, and B. C. Khoo, "A note on supersonic flow control with nanosecond plasma actuator," Phys. Fluids **30**(4), 040907 (2018).

[25]K. Kinefuchi, A. Y. Starikovskiy, and R. B. Miles, "Control of shock-wave/boundary-layer interaction using nanosecond-pulsed plasma actuators," J. Propul. Power **34**(4), 909–919 (2018).

[26]K. Kinefuchi, A. Y. Starikovskiy, and R. B. Miles, "Numerical investigation of nanosecond pulsed plasma actuators for control of shock-wave/boundary-layer separation," Phys. Fluids **30**(10), 106105 (2018).

[27]Z. Zhao, J.-M. Li, J. Zheng, Y. D. Cui, and B. C. Khoo, "Study of shock and induced flow dynamics by nanosecond dielectric-barrier-discharge plasma actuators," AIAA J. **53**(5), 1336–1348 (2015).

[28]Z. Chen, L. Hao, and B. Zhang, "A model for nanosecond pulsed dielectric barrier discharge (NSDBD) actuator and its investigation on the mechanisms of separation control over an airfoil," Sci. China Technol. Sci. **56**, 1055–1065 (2013).

[29]K. Takashima, Y. Zuzeek, W. R. Lempert, and I. V. Adamovich, "Characterization of a surface dielectric barrier discharge plasma sustained by repetitive nanosecond pulses," Plasma Sources Sci. Technol. **20**(5), 055009 (2011).

[30]T. Unfer and J. P. Boeuf, "Modelling of a nanosecond surface discharge actuator," J. Phys. D **42**(19), 194017 (2009).

[31]C.-C. Wang and S. Roy, "Energy and force prediction for a nanosecond pulsed dielectric barrier discharge actuator," J. Appl. Phys. **111**(10), 103302 (2012).

[32]A. Montello, D. Burnette, M. Nishihara, W. R. Lempert, and I. V. Adamovich, "Dynamics of rapid localized heating in nanosecond pulse discharges for high speed flow control," J. Fluid Sci. Technol. **8**(2), 147–159 (2013).

[33]J. G. Zheng, Z. J. Zhao, J. Li, Y. D. Cui, and B. C. Khoo, "Numerical simulation of nanosecond pulsed dielectric barrier discharge actuator in a quiescent flow," Phys. Fluids **26**(3), 036102 (2014).

[34]J. Hao and C.-Y. Wen, "Hypersonic flow over spherically blunted double cones," J. Fluid Mech. **896**, A26 (2020).

[35]B. V. Leer, "Towards the ultimate conservative difference scheme," J. Comput. Phys. **32**, 101–136 (1979).

[36]M. J. Wright, G. V. Candler, and D. Bose, "Data-parallel line relaxation method for the Navier-Stokes equations," AIAA J. **36**(9), 1603–1609 (1998).

[37]J. Hao and C.-Y. Wen, "Effects of vibrational nonequilibrium on hypersonic shock-wave/laminar boundary-layer interactions," Int. Commun. Heat Mass Transfer **97**, 136–142 (2018).

[38]J. Hao, C.-Y. Wen, and J. Wang, "Numerical investigation of hypervelocity shock-wave/boundary-layer interactions over a double-wedge configuration," Int. J. Heat Mass Transfer **138**, 277–292 (2019).

[39]A. C. Aba'a Ndong, N. Zouzou, N. Benard, and E. Moreau, "Geometrical optimization of a surface DBD powered by a nanosecond pulsed high voltage," J. Electrostat. **71**(3), 246–253 (2013).

[40]M. Bleilebens and H. Olivier, "On the influence of elevated surface temperatures on hypersonic shock wave/boundary layer interaction at a heated ramp model," Shock Waves **15**(5), 301–312 (2006).

[41]J. Hao, S. Cao, C.-Y. Wen, and H. Olivier, "Occurrence of global instability in hypersonic compression corner flow," J. Fluid Mech. **919**, A4 (2021).

[42]P. V. Chuvakhov and V. N. Radchenko, "Effect of Görtler-like vortices of various intensity on heat transfer in supersonic compression corner flows," Int. J. Heat Mass Transfer **150**, 119310 (2020).

[43]J. G. Zheng, Y. D. Cui, Z. J. Zhao, J. Li, and B. C. Khoo, "Investigation of airfoil leading edge separation control with nanosecond plasma actuator," Phys. Rev. Fluids **1**(7), 073501 (2016).

13 January 2025 03:48:41